



HAL
open science

Evaluation of atmospheric circulation of CMIP6 models for extreme temperature events using Latent Dirichlet Allocation

Nemo Malhomme, Bérengère Podvin, Davide Faranda, Lionel Mathelin

► **To cite this version:**

Nemo Malhomme, Bérengère Podvin, Davide Faranda, Lionel Mathelin. Evaluation of atmospheric circulation of CMIP6 models for extreme temperature events using Latent Dirichlet Allocation. 2024. hal-04484617v1

HAL Id: hal-04484617

<https://cnrs.hal.science/hal-04484617v1>

Preprint submitted on 29 Feb 2024 (v1), last revised 22 Jul 2024 (v2)

HAL is a multi-disciplinary open access archive for the deposit and dissemination of scientific research documents, whether they are published or not. The documents may come from teaching and research institutions in France or abroad, or from public or private research centers.

L'archive ouverte pluridisciplinaire **HAL**, est destinée au dépôt et à la diffusion de documents scientifiques de niveau recherche, publiés ou non, émanant des établissements d'enseignement et de recherche français ou étrangers, des laboratoires publics ou privés.

1 **Evaluation of atmospheric circulation of CMIP6 models for extreme**
2 **temperature events using Latent Dirichlet Allocation**

3 Nemo Malhomme^{1,2}, Bérengère Podvin³, Davide Faranda¹, Lionel Mathelin²

4 ¹ *ESTIMR, Université Paris-Saclay, CNRS, CEA, UVSQ, Laboratoire des sciences du climat et de*
5 *l'environnement, 91191, Gif-sur-Yvette, France.*

6 ² *LISN, CNRS, Université Paris-Saclay, 91405, Orsay, France.*

7 ³ *Université Paris-Saclay, CNRS, CentraleSupélec, Laboratoire EM2C, 91190, Gif-sur-Yvette,*
8 *France.*

9 *Corresponding author:* Nemo Malhomme, nemo.malhomme@lsce.ipsl.fr

10 ABSTRACT: We study the ability of large-scale circulation models to reproduce extreme tem-
11 perature events. To this end, we use a statistical clustering technique, Latent Dirichlet Allocation
12 (LDA) to characterize sea-level pressure data over the north-Atlantic region. From the ERA5
13 reanalysis dataset, the method extracts a basis of interpretable objects at synoptic scale, that we
14 call “motifs”. Pressure data can be projected onto this basis, yielding motif weights that contain
15 local information about the large-scale atmospheric circulation. We first examine how the weights
16 statistics can be used to characterize extreme events in reanalysis data. We then compare the
17 weights obtained from reanalysis data with those obtained from runs from four CMIP6 models.
18 This allows us to quantify errors on each localized circulation pattern and identify model-agnostic
19 and model-specific errors. On average, large-scale circulation is well predicted by all models, but
20 model errors are increased for extreme events such as heatwaves and cold spells. A significant
21 source of error was found to be associated with Mediterranean motifs for all models in all cases.
22 Each model run can be characterized by a dynamic error associated with the global circulation
23 pattern and a thermodynamic error associated with the predicted temperature. In the general case,
24 this two-dimensional characterization is sufficient to discriminate between models. This remains
25 possible in the cold spell case despite higher internal model variability, while all models perform
26 similarly on heatwaves. The detailed characterization provided by LDA analysis is therefore well
27 suited for model preselection for the study of extreme events.

28 **1. Introduction**

29 Heatwaves and cold spells both cause significant public health and safety risks (Weilhammer
30 et al. (2021)), as well as infrastructure damage (Añel et al. (2017)). They are generally defined
31 as temperature events significantly higher or below average over a period of at least several days.
32 Studies have shown that both the number and the duration of heatwaves in the European region
33 have increased by up to 15% since pre-industrial times (Frich et al. (2002), Alexander et al. (2006)).
34 Examples of severe heatwaves include the European heatwave of 2003 (Fink et al. (2004)), or that
35 of 2018 (McCarthy et al. (2019)). Both events have caused tens of thousands of deaths. While cold
36 spell frequency and intensity have decreased since pre-industrial times (Seneviratne et al. (2021)),
37 they still represent a hazard (López-Bueno et al. (2021)). For instance, we can cite the cold spell
38 of 2017 over the Balkans (Anagnostopoulou et al. (2017)), which had consequent socio-economic
39 impacts. In addition, when occurring during spring, cold spells can have a devastating impact
40 on the development of plants and cause major losses of agricultural yields (Papagiannaki et al.
41 (2014)). One such example is the cold spell of April 2021 described in Vautard et al. (2023b).

42 Heatwaves and cold spells produce anomalies reaching up to $\pm 15^{\circ}\text{C}$ for several consecutive
43 days. This implies that these events cannot be due to local thermodynamic drivers alone. They are
44 explained in large part by changes in atmospheric circulation patterns (Rousi et al. (2022)), namely
45 the ensemble of cyclones and anticyclones affecting a certain region at a given time. Cyclones
46 and anticyclones advect warm or cold air from polar to tropical latitude and vice-versa through the
47 mechanism of baroclinic instability (Wallace and Hobbs (2006)). With the temperature difference
48 between pole and equator reaching up to 60 degrees, cyclones and anticyclones can advect warm
49 and cold air and trigger heatwaves or cold spells. These cyclones and anticyclones evolve most
50 of the time from west to east, because they are embedded in the jet stream. Sporadically, the jet
51 stream creates large meanders that trap cyclones and anticyclones in the same position for several
52 days (Krishnamurti (1961)). This phenomenon, called blocking, can cause persistence of warm
53 or cold conditions in the same areas and trigger heatwave and cold spells (Faranda et al. (2016);
54 Lupo (2021)). Conditions of atmospheric circulation patterns that can cause extreme temperature
55 events are often referred to as their dynamic drivers (Chan et al. (2022)). Simulating the large
56 excursions from the mean temperature responsible for hot and cold prolonged periods in Europe
57 is crucial to understand, anticipate and mitigate the impacts of heatwaves and cold-spells. Global

58 and regional climate models are extensively used for this purpose both in present, past and future
59 climate conditions (Eyring et al. (2016)).

60 However, models still face severe limitations in performing this task. According to the Coupled
61 Model Intercomparison Project (CMIP, Meehl et al. (2000)), the statistical properties of extreme
62 events are reasonably well captured by the models, but challenges persist in reproducing their
63 frequencies and intensities, as well as in capturing local specificities (Kharin et al. (2013), Li
64 et al. (2021)). For example, Vautard et al. (2023a) show that models underestimate the trend of
65 evolution of heatwaves, and Jeong et al. (2021) show that models still underestimate the frequency
66 of cold spells. Models are still unable to accurately reproduce the behavior of the atmosphere
67 and ocean. In particular, they tend to underestimate the warming induced by climate change (van
68 Oldenborgh et al. (2009)), and still contain inaccuracies that affect local circulation patterns (Scaife
69 et al. (2010)), including those linked with extreme heat (D’Andrea et al.), and extreme cold (Davini
70 and D’Andrea (2020)). Despite these biases compared to reality, models have made significant
71 progress over the years. There have been increases in grid resolution, reaching a resolution as high
72 as 1 km in regional models (Lucas-Picher et al. (2021)). Tuning techniques have been developed to
73 reduce biases, such as regarding arctic sea ice cover extent, or the amplitude of Atlantic Meridional
74 Overturning Circulation (Mignot et al. (2021)). Such improvements of the models have resulted in
75 an increased ability to represent observed circulation patterns (Rodrigues et al. (2018)). To assess
76 the advances and the remaining challenges, it is necessary to develop evaluation methodologies
77 that give a comprehensive and accurate measure of a model’s ability to capture extremes and their
78 drivers.

79 Regarding dynamic drivers, it is difficult to study directly atmospheric patterns, owing to their
80 high dimensionality. Several methods attempt to produce a reduced-order representation of the
81 atmospheric circulation. One option is to categorize circulation fields into a set of weather
82 regimes, large-scale quasi-stable states of atmospheric circulation (as first introduced in Rex
83 (1950)). Regimes are effective to describe persistent weather patterns (such as in Vautard (1990)).
84 This is useful to the study of extreme events, since some weather patterns, such as the above-
85 mentioned blockings, can induce extreme events such as cold spells or heatwaves. However, by
86 construction, weather regimes are not localized in space (Michelangeli et al. (1995)). They combine
87 various atmospheric structures that are local, such as, for example, cyclones or anticyclones, into

88 large-scale atmospheric states. This loses the locality and the ability to differentiate between the
89 components. They also typically exist at a time scale too large to define individual extreme events.
90 Another technique is to use climate indices. Climate indices are one-dimensional variables that
91 characterize the state of large-scale patterns, typically oscillations in oceanic circulation patterns
92 that have a large influence over the global and regional climate (Stenseth et al. (2003)). They
93 condense information into a parameter that can be directly studied, and its correlation with all
94 kinds of observables and events measured (de Freitas and Grigorieva (2017)). This is especially
95 useful to study oceanic oscillations, for example (Hanley et al. (2003)). However, since climate
96 indices aggregate a lot of data in a single variable, relevant information about the underlying
97 circulation can be missing.

98 In this study, we show that a technique introduced in Fery et al. (2022) can provide new insight on
99 the atmospheric circulation of extreme weather events and give both local and global quantitative
100 measures of the performance of climate models. The technique relies on a statistical learning tool
101 known as Latent Dirichlet Allocation (LDA) (Blei et al. (2003)). Originally developed for text
102 analysis, it has shown promise in capturing latent structures within complex datasets outside of
103 natural language processing, such as in fluid mechanics (Frihat et al. (2021)), or environmental
104 sciences (Valle et al. (2018)). In Fery et al. (2022), application of the LDA method to NCEP/NCAR
105 sea-level pressure (SLP) maps led to the identification of latent variables, or “motifs”. Those motifs
106 consist of synoptic objects, spatially localized pressure anomalies of the scale of 1000 km. Each
107 map can be represented by a weighted combination of motifs. By monitoring the temporal evolution
108 of the weights, they identified trends in impacts-defined extreme events.

109 In this paper, we show that LDA decomposition can be a useful tool to evaluate the performance
110 of climate models, and in particular to quantify their ability to reproduce extreme temperature
111 events. The paper is organized as follows. In section 2, we present the datasets to be analysed
112 and our methods of analysis. In section 3, motifs extracted from the ERA5 SLP dataset are used
113 to study the synoptic configuration of hot and cold temperature extremes occurring in France.
114 A comparison between the reanalysis and climate models using this synoptic representation is
115 reported in section 4. An evaluation of the climate models is carried out in section 5, based on
116 the joint analysis of the synoptic representation error and the average temperature discrepancy. A
117 conclusion is given in section 6.

118 2. Methods

119 a. Climate data

120 We choose the reanalysis dataset ERA5 (Hersbach et al. (2020)) as the ground truth to train
121 LDA on and compare the models to. Our variable of study is the sea-level pressure (SLP), which
122 contains the synoptic information relevant to a meteorological study, specifically the positions
123 and extents of cyclones and anticyclones. An alternative for these properties would be 500 hPa
124 geopotential height (z500). However, in ERA5 reanalysis data, z500 is computed from SLP rather
125 than simulated directly. The data is converted into anomalies by removing the seasonal cycle,
126 computed for each date as the average of all days corresponding to that date.

127 We chose to evaluate general circulation models, because they represent the physical detail of
128 the atmospheric circulation. At time of writing, the CMIP6 project contains the state of the art
129 in general circulation models. We select four CMIP6 models for which a high number of runs is
130 available: IPSL-CM6A-LR (33 runs) (Boucher et al. (2020)), MIROC6 (50 runs) (Tatebe et al.
131 (2019)), ACCESS-ESM1.5 (29 runs) (Ziehn et al. (2020)), and CanESM5 (25 runs) (Swart et al.
132 (2019)).

133 b. Extreme event definition

134 Among extreme weather events, we study specifically cold spells and heatwaves. It is generally
135 agreed upon that these terms refer to periods of temperatures significantly higher or below average
136 for at least several days. However, any definition more precise is somewhat arbitrary, and there
137 is no general consensus on a specific definition. A definition can be based on socio-economic
138 impacts, on physical indicators, or the events can be automatically categorized through machine
139 learning methods trained on data categorized by hand (such as in Liu et al. (2016)).

140 Since we are interested in evaluating model dynamics, while Fery et al. (2022) uses a definition
141 based on impacts, we prefer to use a physics-based definition. In particular, we define a cold
142 spell (resp. heatwave) as at least 3 consecutive days with average daily temperature below the
143 0.03 quantile (resp. beyond the 0.97 quantile) of average temperatures over the studied period,
144 from 1950 to 2021. Extreme events are defined for specific regions by considering the average
145 temperatures over that region. To illustrate the method, we will consider cold spells and heatwaves

146 occurring in France. The results for five other countries, Italy, Spain, Poland, Germany and the
147 UK, are available in supplemental material.

148 *c. Latent Dirichlet Allocation*

149 Latent Dirichlet Allocation (LDA) is an unsupervised statistical learning method originally
150 devised in the field of natural language processing (Blei et al. (2003)). Its purpose is to extract,
151 from a corpus of written documents, a set of latent variables called “topics” that describe their
152 content. Documents are treated under the “bag of words” hypothesis, which assumes that the
153 ordering of words in documents is irrelevant. A document is defined only by its counts of words
154 belonging to a given vocabulary.

155 The number of topics K is a hyperparameter of the method, equivalent to a number of clusters.
156 The topics are characterized by their distributions over the vocabulary. These are multinomial
157 distributions parameterized by β , with components $\beta_k, k \in [1, K]$ each defining the distribution
158 associated to the topic of index k .

159 LDA is a soft clustering technique: each of the D documents in the corpus is associated with a
160 distribution over the topics. This distribution, denoted c , is a multinomial distribution drawn from
161 a Dirichlet distribution of parameter α .

162 Given the parameters α and β , LDA assumes that each document d of the corpus has been
163 generated as follows:

- 164 • A total number of word positions N in the document d is drawn from a Poisson distribution.
- 165 • A topic composition $c(d)$ is drawn for the document d (see Fig. 1) from a Dirichlet distribution
166 of parameter α .
- 167 • For each word position n in the document:
 - 168 – a topic index $z_{d,n}$ is drawn from $c(d)$.
 - 169 – a word $w_{d,n}$ is drawn from the word-topic distribution $\beta_{z_{d,n}}$.

170 The generative process is summarized in Fig. 2.

171 The joint distribution of all observable and hidden variables, knowing the parameters α and β ,
 172 is:

$$p((w_{d,n})_{d \in [1,D], n \in [1,N]} | \alpha, \beta) = \prod_{d=1}^D \int_c p(c(d) | \alpha) \prod_{n=1}^N \sum_{z_{d,n}=1}^K p(z_{d,n} | c(d)) p(w_{d,n} | z_{d,n}, \beta) dc(d) \quad (1)$$

173 with $c(d)$ drawn from the Dirichlet distribution of parameter α :

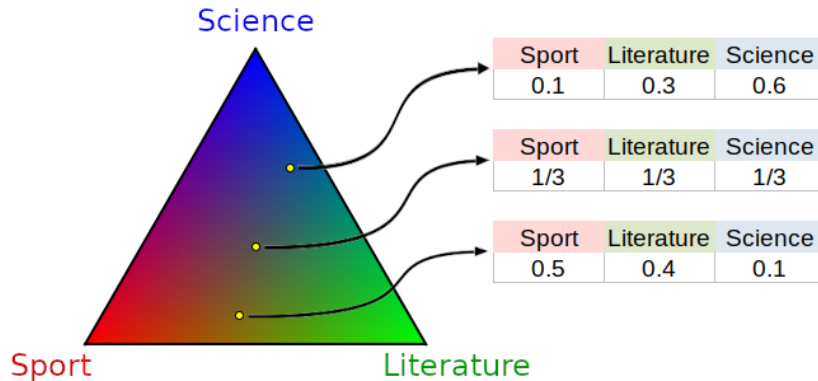
$$p(c(d) | \alpha) = \frac{1}{B(\alpha)} \prod_{k=1}^K c_k(d)^{\alpha_k - 1}, \quad B(\alpha) = \frac{\prod_{k=1}^K \Gamma(\alpha_k)}{\Gamma(\sum_{k=1}^K \alpha_k)} \quad (2)$$

174 $z_{d,n}$ drawn from the multinomial distribution $c(d)$:

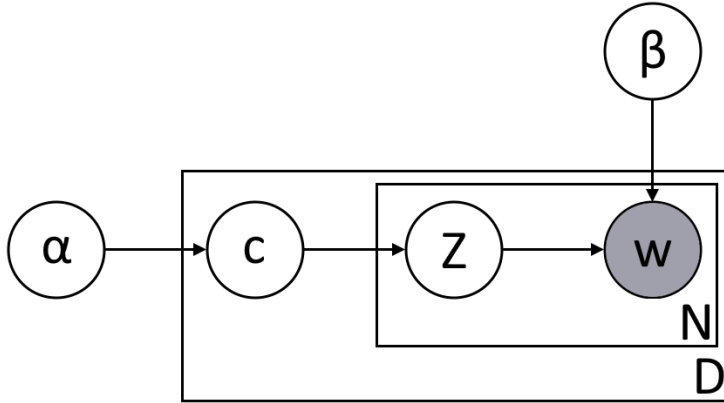
$$p(z_{d,n} = k | c(d)) = c_k(d) \quad (3)$$

175 $w_{d,n}$ drawn from the multinomial distribution β_z :

$$p(w_{d,n} = i | z_{d,n}, \beta) = \beta_{z_{d,n}, i} \quad (4)$$



176 FIG. 1. Example representation of the space of possible topic compositions, on which we define the Dirichlet
 177 probability distribution parameterized by α .



178 FIG. 2. Graphical model representation of the LDA generative process. Circles represent variables, greyed-out
 179 circles being observed variables. Arrows represent the process of drawing a random variable from a distribution.
 180 Rectangles represent reiteration of the process, with D being the number of documents, and N the number of
 181 words in a document.

182 This method is applied to datasets of bidimensional climate variables maps where each spatial
 183 map is reinterpreted as a document. Grid points, or cells, are reinterpreted as the words, with the
 184 list of cells taking the role of the vocabulary. Field values at each cell are reinterpreted as word
 185 counts. In this case, the cell-topics distributions β_k are defined over space and are called “motifs”.
 186 Since the climate variable values are interpreted by LDA as word counts, they have to be digitized
 187 and made non-negative. The real variable maps are therefore separated into two channels, one for
 188 positive and one for negative values. This is equivalent to doubling the grid size over which the
 189 maps are defined. The reader is referred for more details to Fery et al. (2022).

190 Analysis of a corpus of documents with LDA consists in examining the posterior distribution of
 191 the topics β , topic proportions c , and topic assignments z . These are determined via a variational
 192 Bayes approach aiming to maximize the evidence lower bound, which is related to the likelihood
 193 of the observed data. An additional assumption of this approach is that the β_k are assumed to be
 194 drawn from a Dirichlet prior of parameter η . The Dirichlet parameters α and η respectively ensure
 195 the sparsity of the document-topic and the topic-word distributions: there are generally few topics
 196 in each document, and each topic is characterized by high occurrences of a few vocabulary words.

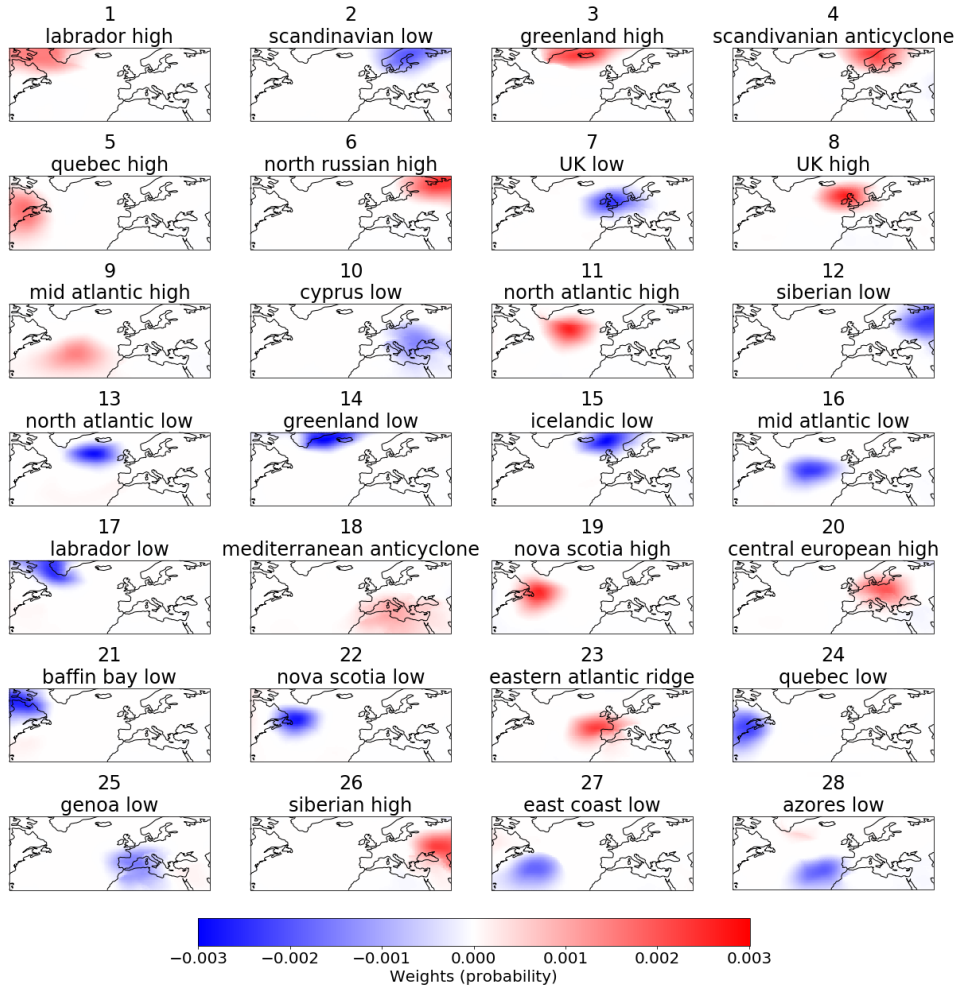
197 This sparsity property makes LDA particularly suited to provide models and decompositions that
198 can be interpreted easily. For more information, see Hoffman et al. (2010).

199 For a given set of D maps, LDA returns motif distributions over grid cells $(\beta_k)_{k \in [1, K]}$, as well
200 as the map compositions $(c_k(d))_{d \in [1, D], k \in [1, K]}$, where $c_k(d)$ denotes the weight of motif k in map
201 d , such that $\forall d \in [1, D], \sum_{k=1}^K c_k(d) = 1$. The motif weights $c(d)$ are always positive, unlike
202 other decompositions such as Principal Component Analysis. The set of distributions $(\beta_k)_{k \in [1, K]}$
203 can be considered as a basis of motifs. Any map P defined on the grid (but not necessarily
204 part of the original set) can be represented in this basis by its K -dimensional motif composition
205 $c(P)$. Different sets of maps can thus be compared efficiently through examination of their motif
206 compositions. In practice, numerical implementation of LDA is carried out with the python module
207 Gensim (Řehůřek and Sojka (2010)).

208 *d. Application of LDA*

209 We apply LDA to ERA5 SLP data from the north-Atlantic region between 22.5° and 70° latitude
210 and 80° and 50° longitude. Although higher resolutions are available, we used a spatial resolution
211 of 1° as it was found to be sufficient to contain all relevant information about circulation patterns on
212 the synoptic scale while maintaining manageable computation times. Our resolution is 48 points
213 in latitude, 130 points in longitude, and we have two channels for positive and negative values.
214 Therefore, the total number of values per map, noted N , is 12480. The temporal correlation time
215 of synoptic circulation patterns is approximately 5 days. The full dataset (which will be referred to
216 as general data) consists of daily averaged SLP anomaly fields from 1950 to 2021. The number of
217 motifs was set to $K = 28$, as previous work (Fery et al. (2022)) showed, using a methodology from
218 the field of dynamic systems (Faranda et al. (2017)), that this was the average local dimension of
219 the SLP anomaly data.

223 These 28 motifs are shown in Fig. 3 and sorted by their average weights in decreasing order. To
224 make discussion easier, names based on their signs and geographical locations were assigned to the
225 motifs. Several motifs in the basis are approximate opposites of one another, such as Labrador high
226 (1) and Labrador low (17), or Genoa low (25) and Mediterranean anticyclone (18). The resulting
227 basis is similar to the one obtained in Fery et al. (2022), which was obtained for different reanalysis
228 datasets at a lower resolution (NCEP/NCAR). Most of the motifs have recognizable equivalents



220 FIG. 3. The basis of 28 motifs learned by LDA from ERA5 SLP anomaly fields. Each motif is defined as a
 221 probability distribution over space, with positive and negative channels. The names were given based on sign
 222 and geographical location.

229 from one basis to the other, although some geographical locations may occasionally differ by a few
 230 hundred kilometers. Motifs can be seen to be analogous to localized synoptic objects of a given
 231 sign, such as cyclones and anticyclones. Therefore, motif weights in a SLP anomaly map directly
 232 measure the contribution of the relevant synoptic objects.

233 LDA offers the possibility of reconstructing maps from a motif composition. The reconstruction
 234 of map P , noted P^* , is obtained based on equation (5).

$$P^* = \|P\|_1 \sum_{k=1}^K c_k(P) \beta_k \quad (5)$$

235 where:

- 236 • β_k is the spatial distribution associated with motif k .
- 237 • $c_k(P)$ is the weight of the k -th motif in the weight vector associated with the pressure map
238 P .
- 239 • $\|P\|_1 = \sum_{i=1}^N |P_i|$ is the ℓ_1 norm of map P over all N grid cells. This term is a renormalization
240 factor, allowing for direct comparison with physical fields.

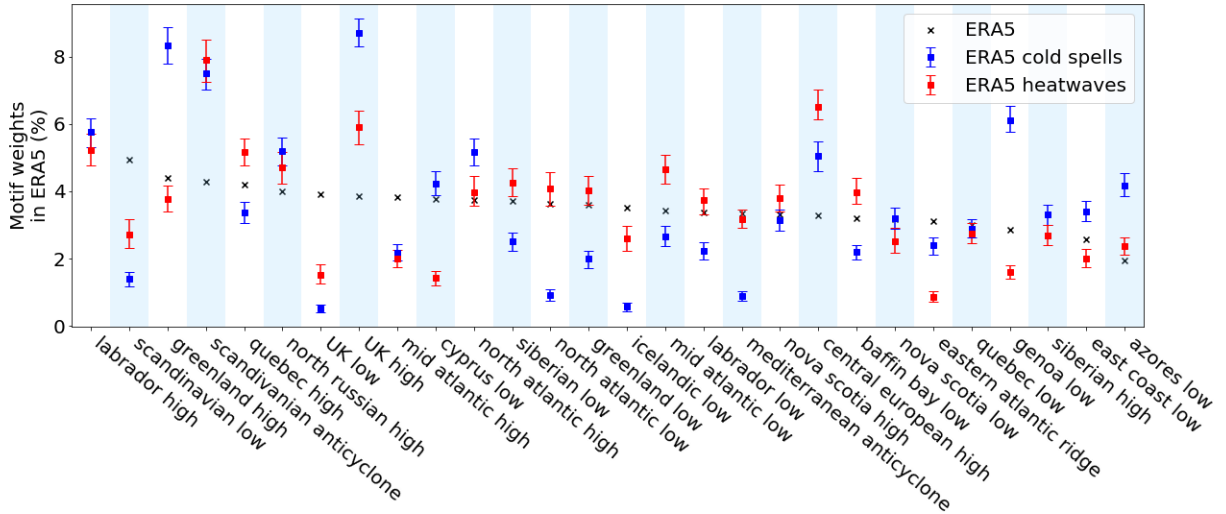
241 In this article, we reconstruct the average compositions of cold spells and heatwaves maps in a
242 given model. In this case, $c_k(P)$ is replaced with $\langle\langle c_k(P) \rangle\rangle$, where $\langle\langle \cdot \rangle\rangle$ designates a conditional
243 average over maps corresponding to the extreme event, and $\|P\|_1$ is replaced with $\|\langle\langle P \rangle\rangle\|_1$.

244 3. Synoptic configuration of extreme events

245 We first use the decomposition into synoptic objects given by LDA to identify the atmospheric
246 circulation patterns associated with cold spells and heatwaves. The patterns associated with extreme
247 temperatures events in one country are expected to differ from those that would cause such events
248 in another. As mentioned above, we focus our study on extreme temperature events occurring in
249 France. The average synoptic configuration of reanalysis fields corresponding to cold spells (resp.
250 heatwaves) is represented and compared to the average configuration of all reanalysis data in Fig.

251 4. Uncertainties are estimated by a resampling method called bootstrapping: many alternative
252 sets of cold spell (resp. heatwave) days are generated by randomly sampling with replacements
253 from the original cold spell (resp. heat wave) data. The average motif weights in these datasets
254 are computed, and the 0.05 and 0.95 quantiles weights for each motif are used as lower and upper
255 errors. We found that statistical convergence was reached with 500 datasets, with quantiles chosen
256 to have a 90% confidence interval.

260 The synoptic configuration of extreme events is different from the average configuration of the
261 general data. Cold spell circulation is dominated by northern anticyclones such as Greenland high,
262 Scandinavian anticyclone and UK high, with more than 6% weights each. Correspondingly, the



257 FIG. 4. Average motif weight in the configuration of ERA5 SLP anomaly fields, in the general case (black), in
 258 the case of cold spells in France (blue), and in the case of heatwaves in France (red). 90% confidence uncertainties
 259 are determined by bootstrapping.

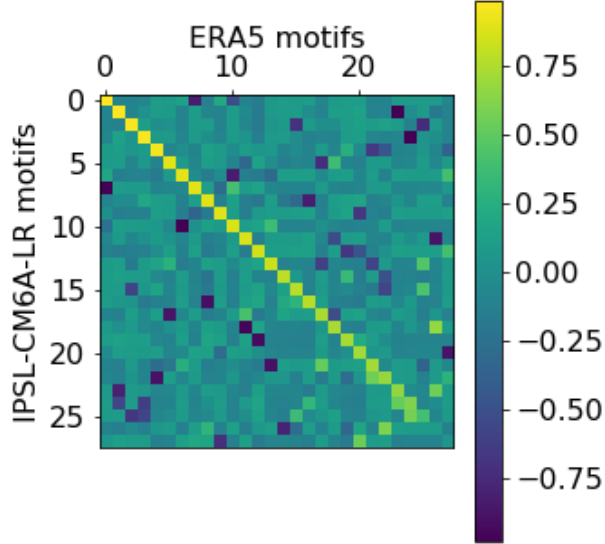
263 low pressure objects over those regions have less than half the weights they have in the general
 264 data. Genoa low is also a key motif in French cold spells, being the fourth most represented
 265 motif. Its opposite, the Mediterranean anticyclone, also has during cold spells half the weights
 266 it has in general. Heatwave circulation is dominated by a smaller set of high-weights motifs,
 267 mainly consisting of Scandinavian anticyclone, and central European high. The UK high is also
 268 more prevalent during heatwaves than in general. Both types of extremes are associated with an
 269 above-average weights of Scandinavian anticyclone and of UK high.

270 4. Evaluation of model representation

271 a. Robustness of the basis

272 We first establish that a unique basis can be used to compare models with reanalysis data. Fig. 5
 273 shows the correlation matrix between the reanalysis data basis and that obtained from a run from a
 274 IPSL-CM6A-LR model, which are respectively associated with cell-motif distributions β and β' .

278 The correlation matrix is obtained as follows: All fields are set to the same 1° resolution by linear
 279 interpolation. For each matrix entry, the Pearson correlation coefficient ρ_{kl} between between motif



275 FIG. 5. Spatial correlation between the motifs of the bases obtained by applying LDA on ERA5 (vertical) and
 276 on IPSL-CM6A-LR run 1 (horizontal). The order of the motifs has been adjusted to put the highest correlations
 277 on the diagonal.

280 k of basis β and motif l of basis β' is computed as shown in equation (6).

$$\rho_{kl} = \frac{\overline{(\beta_k - \bar{\beta}_k)} \overline{(\beta'_l - \bar{\beta}'_l)}}{\sqrt{\overline{(\beta_k - \bar{\beta}_k)^2}} \sqrt{\overline{(\beta'_l - \bar{\beta}'_l)^2}}} \quad (6)$$

281 where $\bar{\cdot}$ designates the spatial average.

282 Motifs were reordered in order to give the same rank in the bases to the motifs with the highest
 283 correlation. For the case considered, 22 out of 28 motifs have a clear equivalent in the other basis
 284 with correlation of at least 0.7 (other choices of models gave similar results). Based on these
 285 results, we consider that the motif basis learned from ERA5 is relevant to represent all model data.

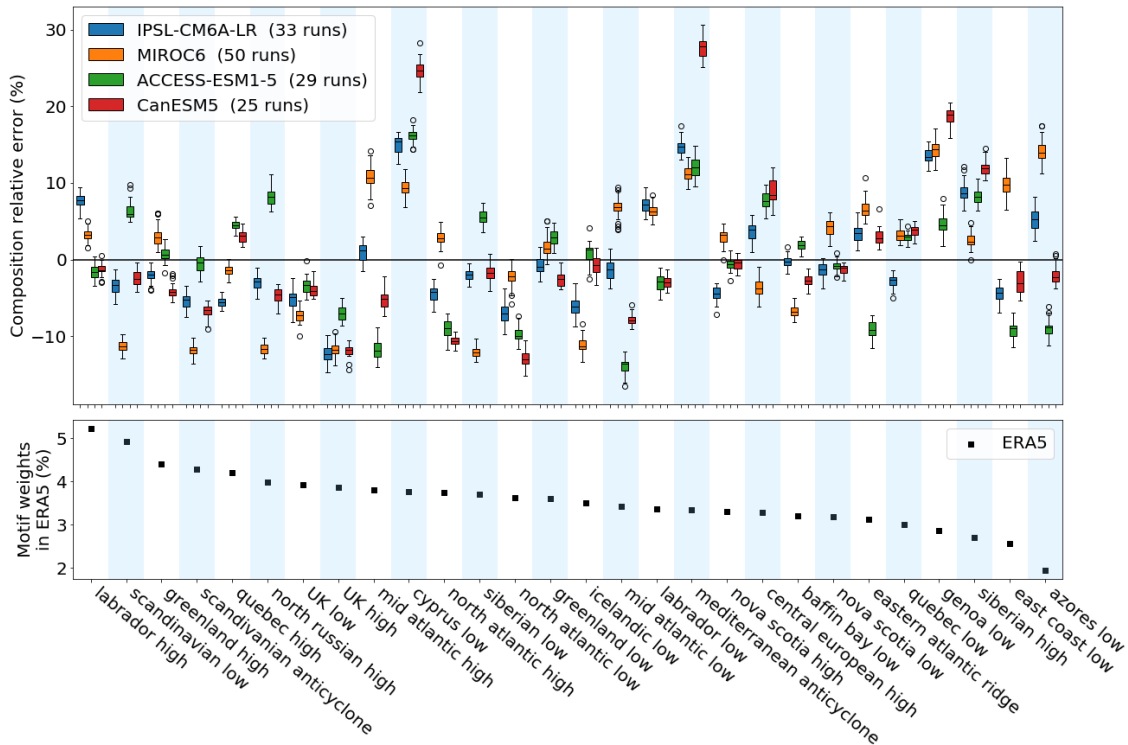
286 *b. General data case*

287 We project each run of the four models onto the motif basis learned from ERA5, then average
 288 the resulting synoptic configuration of the fields over each run. We first consider all fields in the

289 datasets. For each run, the relative difference between the K motif weights in the model and that
 290 in the reanalysis is computed following equation (7).

$$\forall k \in [1, K], E_k = \frac{\langle c_k(P^{m,r}) \rangle - \langle c_k(P) \rangle}{\langle c_k(P) \rangle} \quad (7)$$

291 where P corresponds to reanalysis maps, $P^{m,r}$ corresponds to maps from run r of model m , and
 292 $\langle \cdot \rangle$ designates the average over all maps in the dataset (model run or reanalysis). For each model,
 293 the statistics of the error computed for each model run are shown in Figure 6, using box plots. The
 294 mean weight of the motifs in the reanalysis data is also indicated for comparison.



295 FIG. 6. Top: Relative error on average motif weight between models and ERA5 reanalysis. The box edges
 296 correspond to 1st and 3rd quartiles. The black line is the median. The whiskers extend to the furthest datapoint,
 297 up to 1.5 times the difference between the 1st and 3rd quartiles. Datapoints beyond the whiskers are represented
 298 as colorless circles. Bottom: average motif weight in the synoptic configuration of ERA5 fields.

299 The median relative errors, materialized by the black lines within the boxes, are relatively small.
 300 In particular, the error is less than 15% for the eight most prevalent motifs in the reanalysis.
 301 Overall, models represent well the reanalysis synoptic configuration. Relative errors made by

302 IPSL-CM6A-LR, MIROC6 and ACCESS-ESM1.5, which have resolutions of respectively 38×53 ,
303 34×92 , and 39×69 are all below 20%. We note that the largest error (25%) is observed for
304 CanESM5, which has a resolution of 17×46 . It is possible that these larger errors could be due to
305 its coarser resolution. Moreover, the inner variability of the models (corresponding to the width of
306 the boxes) is typically much smaller than the error (in 96 cases out of the 112 (87.5%), the model's
307 internal variability is lower than its bias). This shows that all runs make similar predictions and
308 also indicates the presence of a bias inherent to each model.

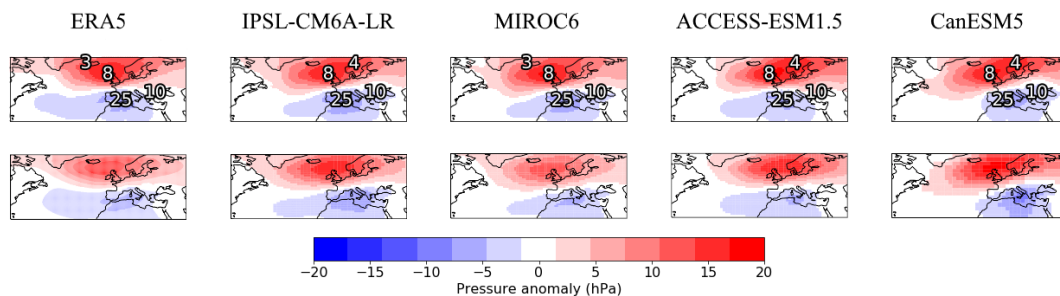
309 In addition, the motifs associated with the largest relative errors tend to be the same from one
310 model to another. A multimodel ensemble mean would therefore not eliminate these biases.
311 The largest errors are made on motifs located on the Mediterranean region. The Cyprus low
312 and Mediterranean anticyclone motifs are over-represented in all runs of all four models. Every
313 model run also over-represents Genoa low and under-represents UK high and low. Finally, the
314 Scandinavian anticyclone is the fourth most prevalent motif in the reanalysis, with an average
315 weight of more than 4% yet all models but ACCESS-ESM1.5 systematically under-represent it.
316 These similarities in the model errors suggest that the origin of the errors could be common to all
317 models.

318 *c. Model representation of cold spells*

319 We study how models capture the circulation patterns of extreme events. For this part, we focus
320 on cold spells occurring in France. The datasets are filtered following the definition proposed in
321 section 2.

322 The fields corresponding to the real and the reconstructed averages are represented in Fig. 7.
323 The real average is obtained by taking a conditional average over all daily fields associated with
324 a cold spell. The reconstructed average is obtained from the average motif compositions of the
325 daily fields included in the conditional average, using equation (5). To identify the most significant
326 motifs associated with each model, the two most prevalent cyclonic and the two most prevalent
327 anticyclonic motifs in each case are annotated on the figure.

331 The overall synoptic structure associated with French cold spells consists of an anticyclonic
332 structure in the north and a cyclonic structure in the south, with a corridor between the two
333 slanted northeast-southwest, passing through the middle of France. For all models, the real average

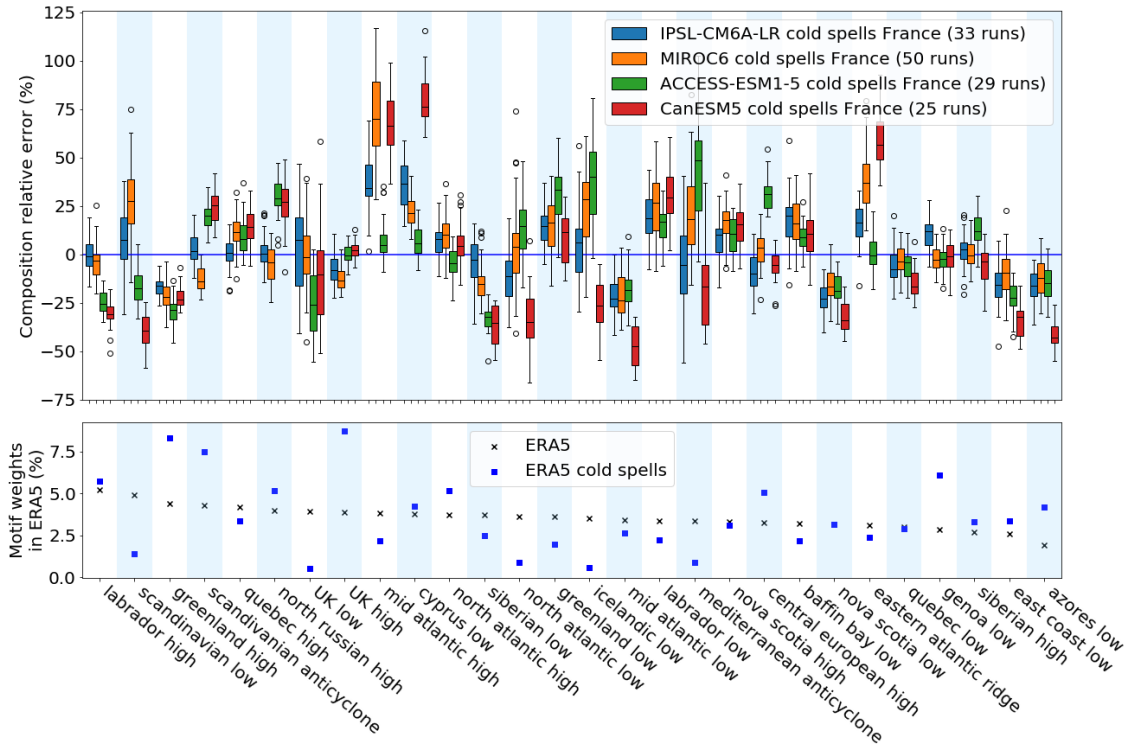


328 FIG. 7. Top line: Reconstruction of the average motif composition of cold spells in France according to
 329 different models (columns). The two cyclones and the two anticyclones with highest average weights in each case
 330 are annotated. Bottom line: Average SLP field for cold spells in France according to different models (columns).

334 is generally similar to its reconstructed average, which shows that LDA captures the synoptic
 335 information contained in the real fields.

336 The model average fields are also in in good agreement with those of ERA5. They have the same
 337 two most prevalent cyclones as ERA5, Cyprus low and Genoa low, and reproduce motif 8, UK
 338 high, as a dominant motif. However some discrepancies are present: all models underestimate the
 339 westward extent of the anticyclonic structure over the Atlantic. Only MIROC6 captures the fact
 340 that Greenland high (motif 3) is more prevalent than Scandinavian anticyclone (motif 4), though as
 341 seen in section 3, Greenland high and Scandinavian anticyclone are both relevant for French cold
 342 spells (near 8% weights). In addition, on CanESM5, Genoa low is too intense, and the cyclonic
 343 structure sees no extension to the west of the Mediterranean sea.

347 For a more detailed analysis, we show for each motif the relative errors in weights between the
 348 reanalyses and the models in the case of cold spells occurring in France, in Fig. 8. The biases
 349 are significantly higher for the cold extremes than for the general case. The variability among the
 350 runs of each models is also higher than for the general case. The five most prevalent reanalysis
 351 motifs during French cold spells are UK high, Greenland high, Scandinavian anticyclone, Genoa
 352 low, Central European high. Most of these motifs are correctly represented by the models. The
 353 significantly higher weights of UK high and Genoa low during cold spells are well captured by all
 354 models with an error within the internal variability of all four models. Central European high is
 355 also well represented by all models except by ACCESS-ESM1-5 which overestimates it by 25%.
 356 The weight of Scandinavian anticyclone high is well captured by IPSL-CM6A-LR and MIROC6,



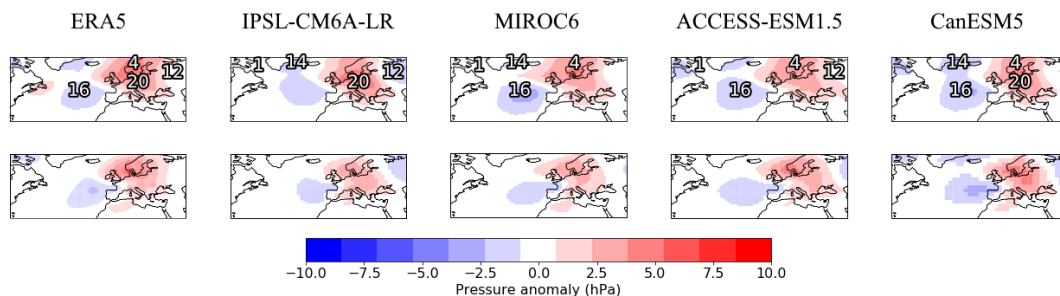
344 FIG. 8. Top: Relative error on average motif weight between models and ERA5 reanalysis in the case of cold
 345 spells occurring in France. Bottom: average motif weight in the synoptic configuration of ERA5 fields, for cold
 346 spells and in the general case.

357 while it is overestimated by 25% by the two other models. All models make about 25% error
 358 on Greenland high. Higher errors are made on less relevant motifs where the reanalysis values
 359 are lower. The most over-represented motifs are Cyprus low and Mid-Atlantic high for all models
 360 except ACCESS-ESM1.5. We note that larger errors are generally observed for the lower resolution
 361 model CAN-ESM5.

362 *d. Model representation of heatwaves*

363 We now focus on heatwaves occurring in France. We represent the real and reconstructed average
 364 heatwave fields in Fig. 9, using the same methodology as in the previous section.

368 The SLP anomaly values are weaker than in the case of cold spells. This is because heatwaves are
 369 more varied in configuration, leading to average error values closer to zero. There are differences
 370 between the real and reconstructed fields. In ERA5 and all models, the anticyclonic structure over



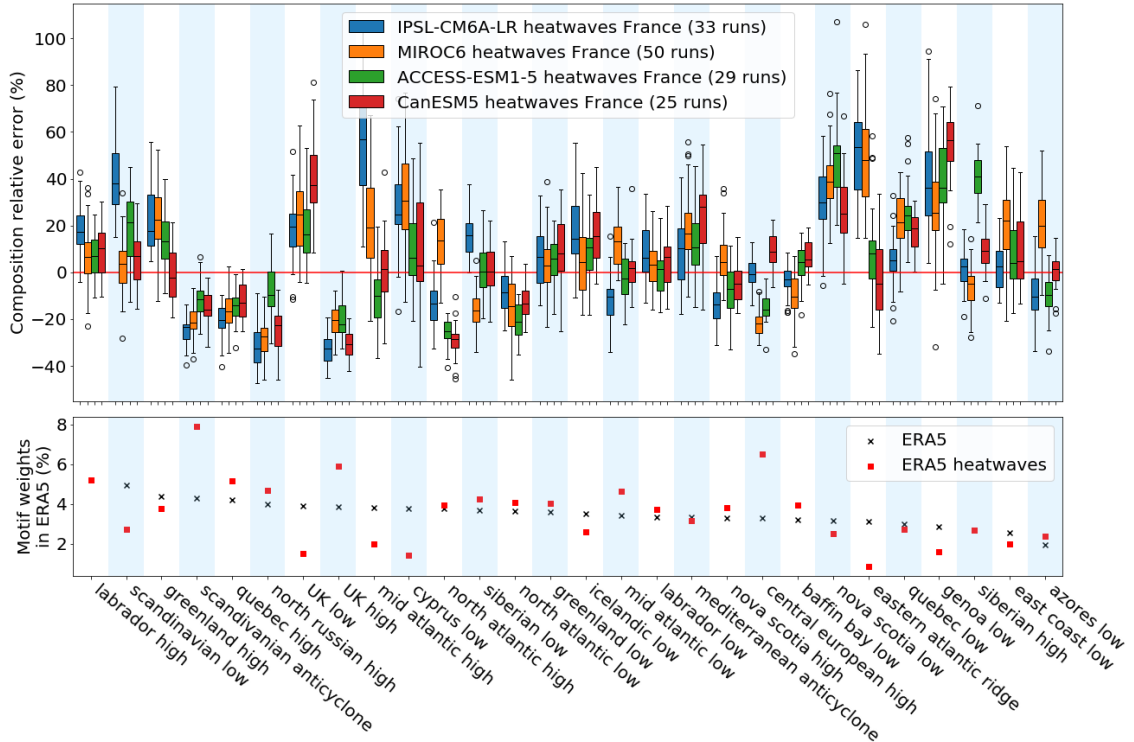
365 FIG. 9. Top line: Reconstruction of the average motif composition of heatwaves in France according to different
 366 models (columns). The two cyclones and the two anticyclones with highest average weights in each case are
 367 annotated. Bottom line: Average SLP field for heatwaves in France according to different models (columns).

371 Europe has a more crescent-like shape around the Atlantic cyclone, that changes into a arrow-like
 372 shape in the LDA reconstruction. Still, the overall structure consisting of anticyclones over northern
 373 and central Europe with a depression over the Atlantic is preserved by LDA reconstruction.

374 Models reproduce the overall structure of ERA5 circulation, with anticyclonic conditions on
 375 northern and central Europe and cyclones over the Atlantic. Models disagree, with ERA5 and each
 376 other, on the shape of those cyclones and the extent of the anticyclonic structure over northern
 377 Atlantic. The most prevalent anticyclones in the reanalysis are the Scandinavian anticyclone (motif
 378 4) and the Central European high (motif 20). Only CanESM5 reproduces this property. For the
 379 other models, this leads to an anticyclonic structure that is weaker in the north for IPSL-CM6A-
 380 LR, in the south for MIROC6, and less intense overall for ACCESS-ESM1.5. The most prevalent
 381 cyclones are Siberian low (motif 12) and Mid-Atlantic low (motif 16). Only ACCESS-ESM1.5
 382 reproduces this property.

383 For a more detailed analysis, we computed relative errors in motif weights between the reanalyses
 384 and the models for heatwaves occurring in France. They are shown in Fig. 10.

388 In the case of heatwaves too, model biases and internal variabilities are higher than in the general
 389 case. Which motifs are or are not relevant is generally well captured by the models. However,
 390 the most relevant motifs tend to be underpredicted by the models. All models except ACCESS-
 391 ESM1.5 under-represent by 20% on average the contribution of the most prevalent motif, which
 392 is the Scandinavian anticyclone. The second most prevalent motif, the central European high,
 393 is well represented by IPSL-CM6A-LR and CanESM5 but under-represented by about 20% by



385 FIG. 10. Top: Relative error on average motif weight between models and ERA5 reanalysis in the case of
 386 heatwaves occurring in France. Bottom: average motif weight in the synoptic configuration of ERA5 fields, for
 387 heatwaves and in the general case.

394 MIROC6 and ACCESS-ESM1.5. UK high, the third most prevalent motif, is under-represented
 395 by 20% or more by almost all runs of all models. In general, motifs that have higher weights
 396 than in the general case tend to be under-represented (as for instance Quebec high and north
 397 Russian high), while motifs that have lower weights (UK low, Nova Scotia low, and Genoa low)
 398 are over-represented. This shows that models underestimate the changes in atmospheric circulation
 399 associated with heatwaves.

400 5. Global dynamic and thermodynamic error

401 a. General data case

402 LDA provides a decomposition of circulation patterns into motifs. Differences in motif weights
 403 provide a quantitative measure of model predictive ability in terms of dynamics. The dynamic
 404 error of run r of model m , $E_p^{m,r}$, is computed according to equation (8).

$$E_P^{m,r} = \sum_{k=1}^K |\langle c_k(P^{m,r}) \rangle - \langle c_k(P) \rangle| \quad (8)$$

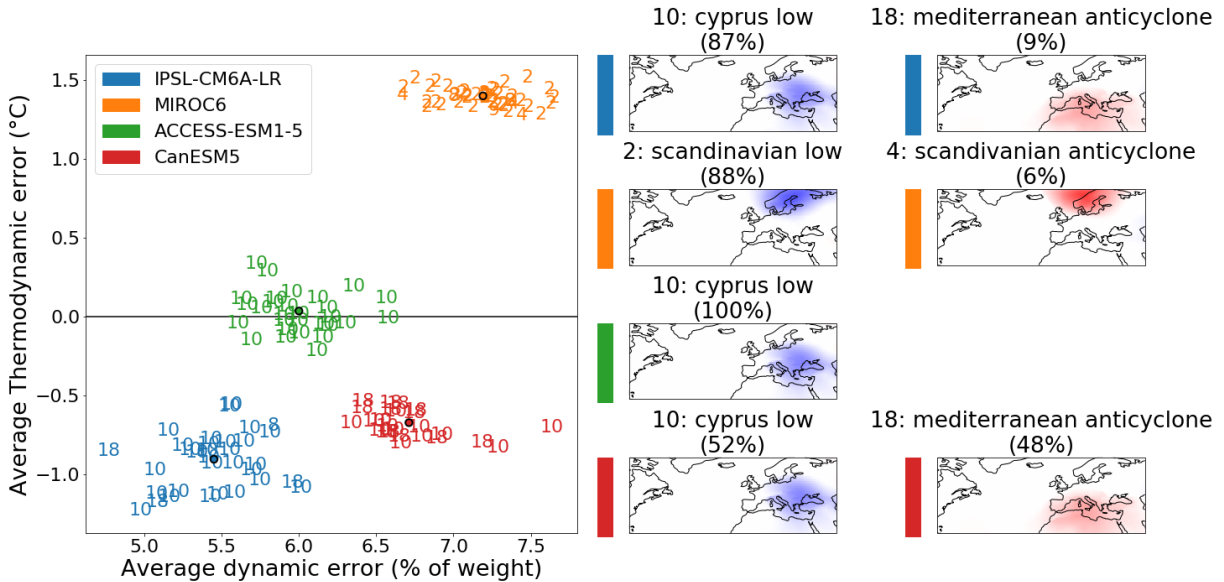
405 The dynamic error can be used to evaluate models comparatively, and produce rankings. An
 406 important question is to determine whether evaluating models based on thermodynamic error, i.e.
 407 the temperature difference between models and reanalysis data, would yield similar results. For
 408 run r of model m , the thermodynamic error is computed as shown in equation (9), with T denoting
 409 reanalysis temperature fields, and $T^{m,r}$ those from run r of model m .

$$E_T^{m,r} = \langle \overline{T^{m,r}} \rangle - \langle \overline{T} \rangle \quad (9)$$

410 Each model run is represented as a point in the error plane $(E_P^{m,r}, E_T^{m,r})$ shown in Fig. 11. In
 411 addition, we annotate for each run the index of the motif which contributes the most to the dynamic
 412 error. For each model, we show on the right of the figure the two motifs that appear most frequently
 413 as the largest contributor to the error of a run (the proportion of runs each motif corresponds
 414 to is indicated between parentheses) - except in the case of ACCESS-ESM1.5, where the largest
 415 contributor is always Cyprus low.

420 Although some overlap between the models would be observed if only one kind of error was
 421 considered, each model can be associated with a well-identified cluster in the 2-D error plane.
 422 MIROC6 is the model with the highest dynamic and thermodynamic error, but with the lowest
 423 thermodynamic variability. Unlike other models, it overpredicts the temperature. In contrast, the
 424 IPSL-CM6A-LR model has the highest thermodynamic variability for a relatively low error (similar
 425 to that of CanESM5), and it also corresponds to the lowest dynamic error. ACCESS-ESM1.5 has
 426 the lowest thermodynamic error for a relatively low dynamic error.

427 As mentioned earlier, each run is annotated with the index of the motif contributing the most
 428 to the dynamic error, which makes it possible to attribute the error to specific motifs and regions
 429 in space. Cyprus low (motif 10) is the least well represented motif for all or almost all runs of
 430 ACCESS-ESM1.5 and IPSL-CM6A-LR, as well as most runs of CanESM5. Another motif that is
 431 occasionally the least well represented in runs of CanESM5 and IPSL-CM6A-LR is Mediterranean
 432 anticyclone (motif 18), the opposite of Cyprus low. Both are eastern Mediterranean motifs.



416 FIG. 11. Run-average thermodynamic model error (average temperature difference with reanalysis), versus
 417 run-average dynamic model error (average motif weights difference with reanalysis). The colored dots indicate
 418 the average of all runs of a model. Each number corresponds to the motif contributing the most to the error in a
 419 given run. The two most frequent such motifs for each model are displayed on the right.

433 We note that these motifs, which contribute the most to the error, are however not the most
 434 prevalent motifs. The associated relative error is therefore necessarily large. This confirms that the
 435 representation of the atmospheric circulation over the eastern Mediterranean region is a significant
 436 issue for all models, particularly for models IPSL-CM6A-LR, ACCESS-ESM1.5, and CanESM5.
 437 MIROC6 appears to differ from other models, as its error on the mean temperature is significantly
 438 higher, and its dynamic error is attributed to different motifs than other models, the Scandinavian
 439 low and Scandinavian anticyclone (motifs 2 and 4). This points to there being different sources of
 440 error between MIROC6 and the other models.

441 *b. Model representation of extreme events*

442 We now consider extreme temperature events and compute the dynamic and thermodynamic
 443 errors associated with heatwaves as well as cold spells. In that case, we eliminate the average bias,
 444 so as to only look at the component specific to extreme events. We therefore define the anomalous
 445 dynamic error $E_{P,ex}^{m,r}$ similarly for heatwaves and cold spells following equation (10).

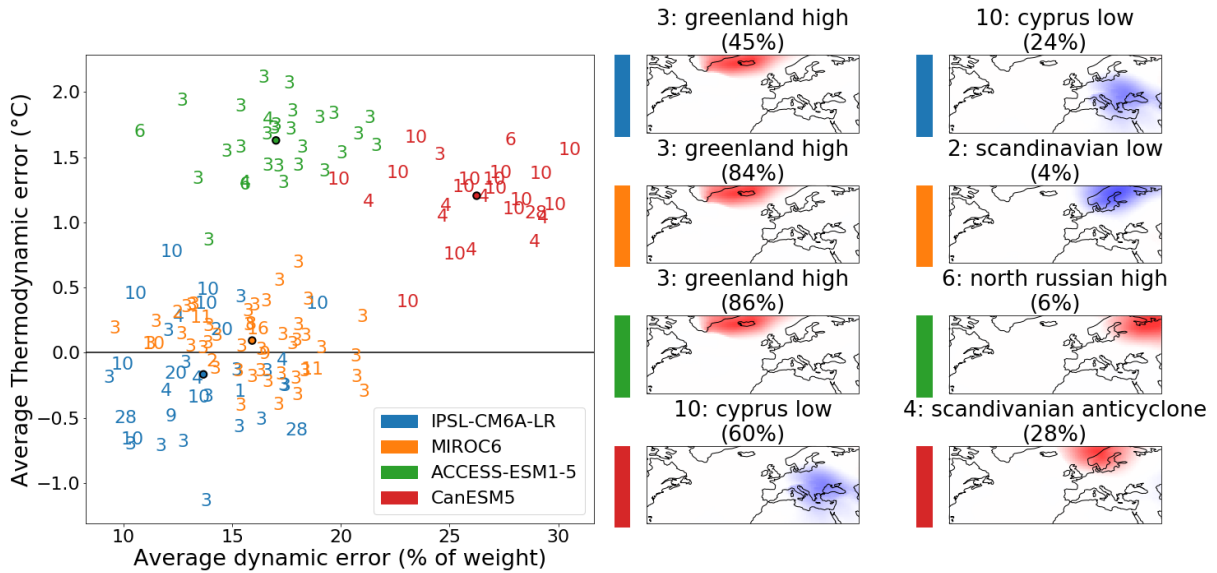
$$E_{P,ex}^{m,r} = \sum_{k=1}^K |\langle \langle c_k(P^{m,r}) \rangle \rangle - \langle \langle c_k(P) \rangle \rangle| - E_P^{m,r} \quad (10)$$

446 The anomalous thermodynamic error $E_{T,ex}^{m,r}$ is defined for heatwaves and cold spells, for run r of
 447 model m following equation (11).

$$E_{T,ex}^{m,r} = \langle \langle \overline{T^{m,r}} \rangle \rangle - \langle \langle \overline{T} \rangle \rangle - E_T^{m,r} \quad (11)$$

448 In subsequent figures, the dynamic and thermodynamic errors represented are only the anomalous
 449 errors defined above. The average errors studied in Fig. 11 are eliminated. However, we note that
 450 the general conclusions reported below did not change when these errors were taken into account.

457 Fig 12 shows model anomalous thermodynamic error against model anomalous dynamic error
 in the case of cold spells occurring in France.



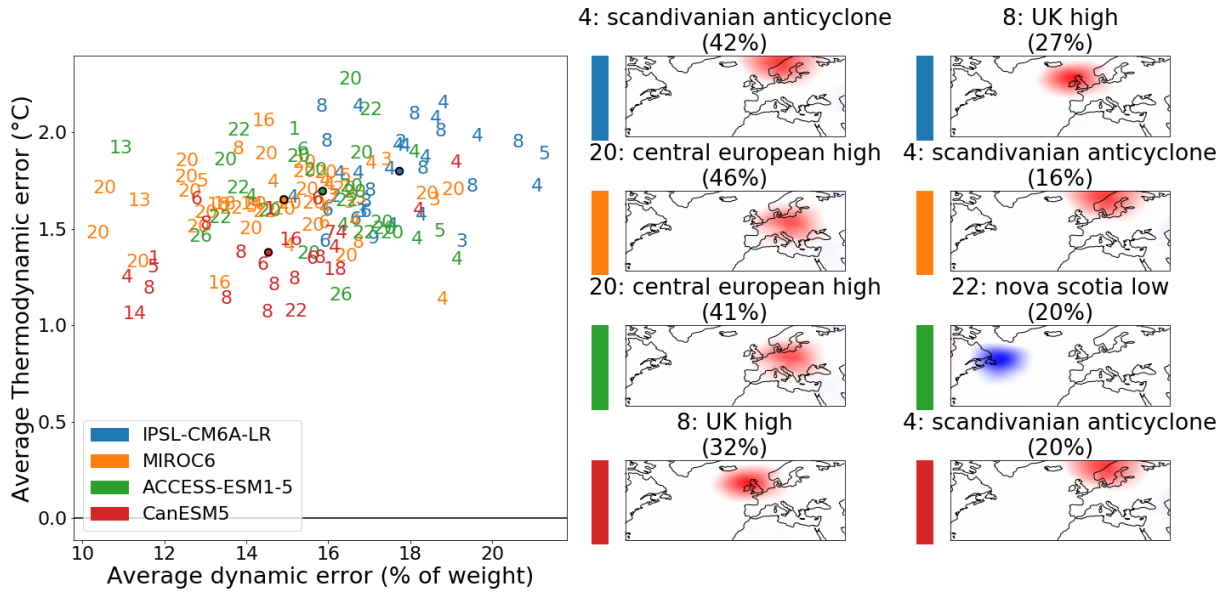
451 FIG. 12. Run-average thermodynamic model error (average temperature difference with reanalysis) on cold
 452 spells in France, versus run-average dynamic model error (average motif weights difference with reanalysis) on
 453 same extremes. We eliminate the errors computed in the general case, so as to look only at errors specific to
 454 extreme events. The colored dots indicate the average of all runs of a model. Each number corresponds to the
 455 motif contributing the most to the error in a given run. The two most frequent such motifs for each model are
 456 displayed on the right.

458 Inner model variability is higher in the cold extreme case than in the full dataset case, both for
459 dynamic and thermodynamic error. There are three distinct clusters in error space, the differences
460 between them being bigger than internal model variabilities. The first cluster corresponds to model
461 CanESM5. It is the model with the highest dynamic error, and has a high thermodynamic error.
462 The second cluster corresponds to model ACCESS-ESM1.5. ACCESS-ESM1.5 has the highest
463 thermodynamic error, underpredicting the lowering of temperature due to cold spells by more than
464 1.5°C on average. Its dynamic error is comparable to that of MIROC6, and both are made in
465 majority on the same motif (Greenland high). The third cluster consists of two models, IPSL-
466 CM6A-LR and MIROC6. With the general bias removed, the temperature value from reanalysis
467 is within the internal variability of both these models. They are also associated with the lowest
468 dynamic error. This cluster appears to be closest to reanalysis. On average, IPSL-CM6A-LR has
469 a slightly lower dynamic error than MIROC6, but the difference is lower than internal variability.

470 Greenland high (motif 3) is the least well represented motif on more than 80% of MIROC6 and
471 ACCESS-ESM1.5 runs, as well as 45% of ISPL-CM6A-LR runs. However this does not signify
472 a major model error in the local atmospheric circulation, as the relative error is small, and the
473 significant contribution simply reflects the predominance of the motif in the composition of cold
474 spells. In contrast, for a majority of CanESM5 runs, as well as 24% of IPSL-CM6A-LR runs, the
475 largest contribution to the dynamic error is due to Cyprus low (motif 10). It is not a particularly
476 dominant motif, but one on which the model makes a significant relative error (75% on median,
477 see Fig. 8). Again this suggests a major flaw in the model representation of local circulation over
478 the Mediterranean.

485 In Fig. 13 we plot model anomalous thermodynamic error against model anomalous dynamic
486 error in the case of heatwaves occurring in France. The inner variability of the models for heatwaves
487 is similar to the cold spell case. However, both thermodynamic and dynamic biases associated
488 with the models are closer, so that in the 2-D error space, regions occupied by each model are
489 overlapping. All four models are associated with similar thermodynamic errors, between +1.0 and
490 +2.5°C - as these biases are all positive, they cannot be removed by use of a multimodel mean.

491 Still, some differences can be made between the models. CanESM5 has the lowest of both types
492 of error on average and IPSL-CM6A-LR the highest, but the differences are lower than model



479 FIG. 13. Run-average thermodynamic model error (average temperature difference with reanalysis) on heat-
 480 waves in France, versus run-average dynamic model error (average motif weights difference with reanalysis)
 481 on same extremes. We eliminate the errors computed in the general case, so as to look only at errors specific
 482 to extreme events. The colored dots indicate the run-average value. Each number corresponds to the motif
 483 contributing the most to the error in a given run. The two most frequent such motifs for each model are displayed
 484 on the right.

493 internal variabilities. In addition, motifs that contribute the most to the error vary significantly
 494 more from run to run than for both general data and cold spells. In particular, no motif dominates
 495 the error in a majority of runs of any model, although some appear more often than others. Central
 496 European high (motif 20) appears most frequently as the most significant contributor to the error
 497 in runs of both MIROC6 and ACCESS-ESM1.5, while Scandinavian anticyclone (motif 4) makes
 498 the largest error contributions in multiple runs of IPSL-CM6A-LR, MIROC6 and CanESM5.
 499 However, we note that both Central European high and Scandinavian anticyclone are dominant
 500 motifs in heatwaves, so their presence does not reflect a significant relative motif error in the
 501 models. To sum up, all models appear to perform comparably for the representation of heat waves,
 502 and it seems difficult to identify specific error characteristics in the models.

503 **6. Conclusion**

504 In this paper, we use a statistical learning method called Latent Dirichlet Allocation (LDA) to
505 study the circulation dynamics of ERA5 reanalysis data and CMIP6 general circulation models.
506 Applied to sea-level pressure fields of the north-Atlantic region from ERA5 data, LDA yields a set
507 of latent variables called “motifs” that are recognizable localized synoptic-scale meteorological
508 objects, such as cyclones and anticyclones. By projecting daily sea-level pressure data onto this
509 basis, we obtain the motif composition, which provides a sparse, low-dimensional representation of
510 atmospheric circulation that can be physically interpreted as the associated synoptic configuration.
511 We showed that synoptic configurations averaged over cold spells and heatwaves were both different
512 from each other and from the average taken over the full data.

513 Using this reanalysis motif basis, we computed the synoptic configuration of runs from 4 different
514 CMIP6 models. Evaluation of the models was based on comparing the statistics of model synoptic
515 configurations with that of reanalysis ones. Differences between models and reanalysis could
516 then be directly attributed to changes in the average weights of individual motifs. This local
517 characterization of the circulation could help discriminate between model predictions, and also
518 help identify the origin of model limitations. Generally speaking, a good agreement was found for
519 general data, while discrepancies were larger for extreme events. In all cases, the largest source
520 of model error was due to the circulation over the eastern Mediterranean region. Moreover, all
521 models tended to underestimate the changes in atmospheric circulation associated with heat waves.

522 A global dynamic error, based on synoptic configuration differences with reanalysis, was com-
523 pared with a thermodynamic error, based on the differences in average temperature. These two
524 indicators were found to be sufficient to help discriminate between models when considering gen-
525 eral data. Discriminating between models was still possible in the cold spell case, while models
526 performed comparably on heatwaves. This method could therefore be used to determine whether
527 specific models are best suited to the study of a given type of event. Characterization of the error
528 is also relevant to knowing how to aggregate model data, and identifying the biases that can be
529 eliminated this way.

530 **7. Acknowledgements**

531 This work is supported by CNRS-MITI (80 PRIME project ACLIM). We thank Robin Noyelle,
532 Camille Cadiou and Mireia Ginesta-Fernandez for their help in processing the data.

533 **8. Availability statement**

534 This work makes use of the Gensim python module, which is publicly available for download
535 through the pip interface. ERA5 reanalysis data are made publicly available by the Copernicus
536 program, see <https://doi.org/10.24381/cds.143582cf>. Model datasets used in this article are sim-
537 ulations from the CMIP6 project for the “historical” experiment, by the models IPSL-CM6A-LR,
538 MIROC6, ACCESS-ESM1.5 and CMIP6. The data is publicly available thanks to the World
539 Climate Research Programme, and can be found at: <https://esgf-node.llnl.gov/search/cmip6>.

540 **9. References**

541 **References**

- 542 L. V. Alexander, X. Zhang, T. C. Peterson, J. Caesar, B. Gleason, A. M. G. Klein Tank,
543 M. Haylock, D. Collins, B. Trewin, F. Rahimzadeh, A. Tagipour, K. Rupa Kumar, J. Re-
544 vadekar, G. Griffiths, L. Vincent, D. B. Stephenson, J. Burn, E. Aguilar, M. Brunet, M. Tay-
545 lor, M. New, P. Zhai, M. Rusticucci, and J. L. Vazquez-Aguirre. Global observed changes
546 in daily climate extremes of temperature and precipitation. *Journal of Geophysical Re-*
547 *search: Atmospheres*, 111(D5), 2006. ISSN 2156-2202. doi: 10.1029/2005JD006290.
548 URL <https://onlinelibrary.wiley.com/doi/abs/10.1029/2005JD006290>. _eprint:
549 <https://onlinelibrary.wiley.com/doi/pdf/10.1029/2005JD006290>.
- 550 C. Anagnostopoulou, K. Tolika, G. Lazoglou, and P. Maheras. The Exceptionally Cold January of
551 2017 over the Balkan Peninsula: A Climatological and Synoptic Analysis. *Atmosphere*, 8(12):
552 252, Dec. 2017. ISSN 2073-4433. doi: 10.3390/atmos8120252. URL <https://www.mdpi.com/2073-4433/8/12/252>. Number: 12 Publisher: Multidisciplinary Digital Publishing
553 Institute.
554
- 555 J. A. Añel, M. Fernández-González, X. Labandeira, X. López-Otero, and L. De la Torre. Impact
556 of Cold Waves and Heat Waves on the Energy Production Sector. *Atmosphere*, 8(11):209,
557 Nov. 2017. ISSN 2073-4433. doi: 10.3390/atmos8110209. URL [https://www.mdpi.com/](https://www.mdpi.com/2073-4433/8/11/209)
558 [2073-4433/8/11/209](https://www.mdpi.com/2073-4433/8/11/209). Number: 11 Publisher: Multidisciplinary Digital Publishing Institute.
- 559 D. M. Blei, A. Y. Ng, and M. I. Jordan. Latent dirichlet allocation. *The Journal of Machine*
560 *Learning Research*, 3(null):993–1022, Mar. 2003. ISSN 1532-4435.
- 561 O. Boucher, J. Servonnat, A. L. Albright, O. Aumont, Y. Balkanski, V. Bastrikov, S. Bekki, R. Bon-
562 net, S. Bony, L. Bopp, P. Braconnot, P. Brockmann, P. Cadule, A. Caubel, F. Cheruy, F. Codron,
563 A. Cozic, D. Cugnet, F. D’Andrea, P. Davini, C. de Lavergne, S. Denvil, J. Deshayes, M. Dev-
564 illiers, A. Ducharne, J.-L. Dufresne, E. Dupont, C. Éthé, L. Fairhead, L. Falletti, S. Flavoni,
565 M.-A. Foujols, S. Gardoll, G. Gastineau, J. Ghattas, J.-Y. Grandpeix, B. Guenet, E. Guez, Li-
566 onel, E. Guilyardi, M. Guimberteau, D. Hauglustaine, F. Hourdin, A. Idelkadi, S. Joussaume,
567 M. Kageyama, M. Khodri, G. Krinner, N. Lebas, G. Levvasseur, C. Lévy, L. Li, F. Lott,

568 T. Lurton, S. Luysaert, G. Madec, J.-B. Madeleine, F. Maignan, M. Marchand, O. Marti,
569 L. Mellul, Y. Meurdesoif, J. Mignot, I. Musat, C. Ottlé, P. Peylin, Y. Planton, J. Polcher,
570 C. Rio, N. Rochetin, C. Rousset, P. Sepulchre, A. Sima, D. Swingedouw, R. Thiéblemont,
571 A. K. Traore, M. Vancoppenolle, J. Vial, J. Vialard, N. Viovy, and N. Vuichard. Presenta-
572 tion and Evaluation of the IPSL-CM6A-LR Climate Model. *Journal of Advances in Modeling*
573 *Earth Systems*, 12(7):e2019MS002010, 2020. ISSN 1942-2466. doi: 10.1029/2019MS002010.
574 URL <https://onlinelibrary.wiley.com/doi/abs/10.1029/2019MS002010>. _eprint:
575 <https://onlinelibrary.wiley.com/doi/pdf/10.1029/2019MS002010>.

576 P. W. Chan, J. L. Catto, and M. Collins. Heatwave–blocking relation change likely dominates over
577 decrease in blocking frequency under global warming. *npj Climate and Atmospheric Science*, 5
578 (1):68, 2022.

579 P. Davini and F. D’Andrea. From CMIP3 to CMIP6: Northern Hemisphere Atmospheric Block-
580 ing Simulation in Present and Future Climate. *Journal of Climate*, 33(23):10021–10038,
581 Dec. 2020. ISSN 0894-8755, 1520-0442. doi: 10.1175/JCLI-D-19-0862.1. URL <https://journals.ametsoc.org/view/journals/clim/33/23/jclid190862.xml>. Publisher:
582 American Meteorological Society Section: Journal of Climate.

584 C. R. de Freitas and E. A. Grigorieva. A comparison and appraisal of a comprehensive range
585 of human thermal climate indices. *International Journal of Biometeorology*, 61(3):487–512,
586 Mar. 2017. ISSN 1432-1254. doi: 10.1007/s00484-016-1228-6. URL [https://doi.org/10.](https://doi.org/10.1007/s00484-016-1228-6)
587 [1007/s00484-016-1228-6](https://doi.org/10.1007/s00484-016-1228-6).

588 F. D’Andrea, J.-P. Duvel, G. Rivière, R. Vautard, J. Cattiaux, D. Coumou, D. Faranda, T. Happé,
589 A. Ribes, and P. Yiou. Summer Deep Depressions Increase Over the North Atlantic.

590 V. Eyring, S. Bony, G. A. Meehl, C. A. Senior, B. Stevens, R. J. Stouffer, and K. E. Taylor.
591 Overview of the Coupled Model Intercomparison Project Phase 6 (CMIP6) experimental design
592 and organization. *Geoscientific Model Development*, 9(5):1937–1958, May 2016. ISSN 1991-
593 959X. doi: 10.5194/gmd-9-1937-2016. URL [https://gmd.copernicus.org/articles/
594 9/1937/2016/gmd-9-1937-2016.html](https://gmd.copernicus.org/articles/9/1937/2016/gmd-9-1937-2016.html). Publisher: Copernicus GmbH.

- 595 D. Faranda, G. Masato, N. Moloney, Y. Sato, F. Daviaud, B. Dubrulle, and P. Yiou. The switching
596 between zonal and blocked mid-latitude atmospheric circulation: a dynamical system perspec-
597 tive. *Climate Dynamics*, 47:1587–1599, 2016.
- 598 D. Faranda, G. Messori, and P. Yiou. Dynamical proxies of North Atlantic predictability and
599 extremes. *Scientific Reports*, 7(1):41278, Jan. 2017. ISSN 2045-2322. doi: 10.1038/srep41278.
600 URL <https://www.nature.com/articles/srep41278>. Number: 1 Publisher: Nature Pub-
601 lishing Group.
- 602 L. Fery, B. Dubrulle, B. Podvin, F. Pons, and D. Faranda. Learning a Weather Dictio-
603 nary of Atmospheric Patterns Using Latent Dirichlet Allocation. *Geophysical Research*
604 *Letters*, 49(9):e2021GL096184, 2022. ISSN 1944-8007. doi: 10.1029/2021GL096184.
605 URL <https://onlinelibrary.wiley.com/doi/abs/10.1029/2021GL096184>. _eprint:
606 <https://onlinelibrary.wiley.com/doi/pdf/10.1029/2021GL096184>.
- 607 A. H. Fink, T. Brücher, A. Krüger, G. C. Leckebusch, J. G. Pinto, and U. Ulbrich. The 2003
608 European summer heatwaves and drought - synoptic diagnosis and impacts. *Weather*, 59(8):209–
609 216, 2004. ISSN 0043-1656. doi: 10.1256/wea.73.04. URL [https://oceanrep.geomar.
610 de/id/eprint/30311/](https://oceanrep.geomar.de/id/eprint/30311/). Number: 8 Publisher: Wiley-Blackwell.
- 611 P. Frich, L. V. Alexander, P. Della-Marta, B. Gleason, M. Haylock, A. M. G. K. Tank, and
612 T. Peterson. Observed coherent changes in climatic extremes during the second half of the
613 twentieth century. *Climate Research*, 19(3):193–212, Jan. 2002. ISSN 0936-577X, 1616-
614 1572. doi: 10.3354/cr019193. URL [https://www.int-res.com/abstracts/cr/v19/n3/
615 p193-212/](https://www.int-res.com/abstracts/cr/v19/n3/p193-212/).
- 616 M. Frihat, B. Podvin, L. Mathelin, Y. Fraigneau, and F. Yvon. Coherent structure identification
617 in turbulent channel flow using Latent Dirichlet Allocation. *Journal of Fluid Mechanics*, 920:
618 A27, Aug. 2021. ISSN 0022-1120, 1469-7645. doi: 10.1017/jfm.2021.444. URL [http:
619 //arxiv.org/abs/2005.10010](http://arxiv.org/abs/2005.10010). arXiv: 2005.10010.
- 620 D. E. Hanley, M. A. Bourassa, J. J. O’Brien, S. R. Smith, and E. R. Spade. A Quan-
621 titative Evaluation of ENSO Indices. *Journal of Climate*, 16(8):1249–1258, Apr. 2003.
622 ISSN 0894-8755, 1520-0442. doi: 10.1175/1520-0442(2003)16<1249:AQEOEI>2.0.CO;2.

623 URL https://journals.ametsoc.org/view/journals/clim/16/8/1520-0442_2003_
624 [16_1249_aqeoie_2.0.co_2.xml](https://journals.ametsoc.org/view/journals/clim/16/8/1520-0442_2003_16_1249_aqeoie_2.0.co_2.xml). Publisher: American Meteorological Society Section:
625 Journal of Climate.

626 H. Hersbach, B. Bell, P. Berrisford, S. Hirahara, A. Horányi, J. Muñoz-Sabater, J. Nicolas,
627 C. Peubey, R. Radu, D. Schepers, A. Simmons, C. Soci, S. Abdalla, X. Abellan, G. Balsamo,
628 P. Bechtold, G. Biavati, J. Bidlot, M. Bonavita, G. De Chiara, P. Dahlgren, D. Dee, M. Dia-
629 mantakis, R. Dragani, J. Flemming, R. Forbes, M. Fuentes, A. Geer, L. Haimberger, S. Healy,
630 R. J. Hogan, E. Hólm, M. Janisková, S. Keeley, P. Laloyaux, P. Lopez, C. Lupu, G. Radnoti,
631 P. de Rosnay, I. Rozum, F. Vamborg, S. Villaume, and J.-N. Thépaut. The ERA5 global reanal-
632 ysis. *Quarterly Journal of the Royal Meteorological Society*, 146(730):1999–2049, 2020. ISSN
633 1477-870X. doi: 10.1002/qj.3803. URL [https://onlinelibrary.wiley.com/doi/abs/](https://onlinelibrary.wiley.com/doi/abs/10.1002/qj.3803)
634 [10.1002/qj.3803](https://onlinelibrary.wiley.com/doi/abs/10.1002/qj.3803). eprint: <https://onlinelibrary.wiley.com/doi/pdf/10.1002/qj.3803>.

635 M. Hoffman, F. Bach, and D. Blei. Online Learning for Latent Dirichlet Allocation.
636 In *Advances in Neural Information Processing Systems*, volume 23. Curran Associates,
637 Inc., 2010. URL [https://proceedings.neurips.cc/paper_files/paper/2010/hash/](https://proceedings.neurips.cc/paper_files/paper/2010/hash/71f6278d140af599e06ad9bf1ba03cb0-Abstract.html)
638 [71f6278d140af599e06ad9bf1ba03cb0-Abstract.html](https://proceedings.neurips.cc/paper_files/paper/2010/hash/71f6278d140af599e06ad9bf1ba03cb0-Abstract.html).

639 D. I. Jeong, B. Yu, and A. J. Cannon. Links between atmospheric blocking and North American
640 winter cold spells in two generations of Canadian Earth System Model large ensembles. *Climate*
641 *Dynamics*, 57(7):2217–2231, Oct. 2021. ISSN 1432-0894. doi: 10.1007/s00382-021-05801-0.
642 URL <https://doi.org/10.1007/s00382-021-05801-0>.

643 V. V. Kharin, F. W. Zwiers, X. Zhang, and M. Wehner. Changes in temperature and precipitation ex-
644 tremes in the CMIP5 ensemble. *Climatic Change*, 119(2):345–357, July 2013. ISSN 1573-1480.
645 doi: 10.1007/s10584-013-0705-8. URL <https://doi.org/10.1007/s10584-013-0705-8>.

646 T. N. Krishnamurti. The subtropical jet stream of winter. *Journal of the Atmospheric Sciences*, 18
647 (2):172–191, 1961.

648 C. Li, F. Zwiers, X. Zhang, G. Li, Y. Sun, and M. Wehner. Changes in Annual Extremes of
649 Daily Temperature and Precipitation in CMIP6 Models. *Journal of Climate*, 34(9):3441–3460,
650 May 2021. ISSN 0894-8755, 1520-0442. doi: 10.1175/JCLI-D-19-1013.1. URL <https://doi.org/10.1175/JCLI-D-19-1013.1>.

651 //journals.ametsoc.org/view/journals/clim/34/9/JCLI-D-19-1013.1.xml. Pub-
652 lisher: American Meteorological Society Section: Journal of Climate.

653 Y. Liu, E. Racah, Prabhat, J. Correa, A. Khosrowshahi, D. Lavers, K. Kunkel, M. Wehner, and
654 W. Collins. Application of Deep Convolutional Neural Networks for Detecting Extreme Weather
655 in Climate Datasets. *arXiv:1605.01156 [cs]*, May 2016. URL <http://arxiv.org/abs/1605.01156>.
656 arXiv: 1605.01156.

657 P. Lucas-Picher, D. Argüeso, E. Brisson, Y. Trambly, P. Berg, A. Lemonsu, S. Kotlarski, and
658 C. Caillaud. Convection-permitting modeling with regional climate models: Latest develop-
659 ments and next steps. *WIREs Climate Change*, 12(6):e731, 2021. ISSN 1757-7799. doi: 10.
660 1002/wcc.731. URL <https://onlinelibrary.wiley.com/doi/abs/10.1002/wcc.731>.
661 _eprint: <https://onlinelibrary.wiley.com/doi/pdf/10.1002/wcc.731>.

662 A. R. Lupo. Atmospheric blocking events: A review. *Annals of the New York Academy of Sciences*,
663 1504(1):5–24, 2021.

664 J. A. López-Bueno, M. Navas-Martín, J. Díaz, I. J. Mirón, M. Y. Luna, G. Sánchez-Martínez,
665 D. Culqui, and C. Linares. The effect of cold waves on mortality in urban and rural areas
666 of Madrid. *Environmental Sciences Europe*, 33(1):72, June 2021. ISSN 2190-4715. doi:
667 10.1186/s12302-021-00512-z. URL <https://doi.org/10.1186/s12302-021-00512-z>.

668 M. McCarthy, N. Christidis, N. Dunstone, D. Fereday, G. Kay, A. Klein-Tank, J. Lowe,
669 J. Petch, A. Scaife, and P. Stott. Drivers of the UK summer heatwave of
670 2018. *Weather*, 74(11):390–396, 2019. ISSN 1477-8696. doi: 10.1002/wea.
671 3628. URL <https://onlinelibrary.wiley.com/doi/abs/10.1002/wea.3628>. _eprint:
672 <https://onlinelibrary.wiley.com/doi/pdf/10.1002/wea.3628>.

673 G. A. Meehl, G. J. Boer, C. Covey, M. Latif, and R. J. Stouffer. The Coupled Model Intercomparison
674 Project (CMIP). *Bulletin of the American Meteorological Society*, 81(2):313–318, Feb. 2000.
675 ISSN 0003-0007, 1520-0477. doi: 10.1175/1520-0477(2000)081<0313:TCMIPC>2.3.CO;
676 2. URL [http://journals.ametsoc.org/doi/10.1175/1520-0477\(2000\)081<0313:
677 TCMIPC>2.3.CO;2](http://journals.ametsoc.org/doi/10.1175/1520-0477(2000)081<0313:TCMIPC>2.3.CO;2).

- 678 P.-A. Michelangeli, R. Vautard, and B. Legras. Weather Regimes: Recurrence and
679 Quasi Stationarity. *Journal of the Atmospheric Sciences*, 52(8):1237–1256, Apr. 1995.
680 ISSN 0022-4928, 1520-0469. doi: 10.1175/1520-0469(1995)052<1237:WRRMQS>2.0.CO;2.
681 URL [https://journals.ametsoc.org/view/journals/atsc/52/8/1520-0469_1995_](https://journals.ametsoc.org/view/journals/atsc/52/8/1520-0469_1995_052_1237_wrraqs_2_0_co_2.xml)
682 [052_1237_wrraqs_2_0_co_2.xml](https://journals.ametsoc.org/view/journals/atsc/52/8/1520-0469_1995_052_1237_wrraqs_2_0_co_2.xml). Publisher: American Meteorological Society Section:
683 Journal of the Atmospheric Sciences.
- 684 J. Mignot, F. Hourdin, J. Deshayes, O. Boucher, G. Gastineau, I. Musat, M. Vancoppenolle,
685 J. Servonnat, A. Caubel, F. Ch eruy, S. Denvil, J.-L. Dufresne, C. Eth e, L. Fairhead, M.-
686 A. Foujols, J.-Y. Grandpeix, G. Levavasseur, O. Marti, M. Menary, C. Rio, C. Rousset, and
687 Y. Silvy. The Tuning Strategy of IPSL-CM6A-LR. *Journal of Advances in Modeling Earth*
688 *Systems*, 13(5):e2020MS002340, 2021. ISSN 1942-2466. doi: 10.1029/2020MS002340.
689 URL <https://onlinelibrary.wiley.com/doi/abs/10.1029/2020MS002340>. _eprint:
690 <https://onlinelibrary.wiley.com/doi/pdf/10.1029/2020MS002340>.
- 691 K. Papagiannaki, K. Lagouvardos, V. Kotroni, and G. Papagiannakis. Agricultural losses related to
692 frost events: use of the 850 hPa level temperature as an explanatory variable of the damage cost.
693 *Natural Hazards and Earth System Sciences*, 14(9):2375–2386, Sept. 2014. ISSN 1561-8633.
694 doi: 10.5194/nhess-14-2375-2014. URL [https://nhess.copernicus.org/articles/14/](https://nhess.copernicus.org/articles/14/2375/2014/)
695 [2375/2014/](https://nhess.copernicus.org/articles/14/2375/2014/). Publisher: Copernicus GmbH.
- 696 R. Řeh urek and P. Sojka. Software Framework for Topic Modelling with Large Corpora. In
697 *Proceedings of the LREC 2010 Workshop on New Challenges for NLP Frameworks*, pages
698 45–50, Valletta, Malta, May 2010. ELRA. <http://is.muni.cz/publication/884893/en>.
- 699 D. F. Rex. Blocking Action in the Middle Troposphere and its Effect upon Regional Climate.
700 *Tellus*, 2(4):275–301, Jan. 1950. ISSN 0040-2826. doi: 10.3402/tellusa.v2i4.8603. URL
701 <https://doi.org/10.3402/tellusa.v2i4.8603>. Publisher: Taylor & Francis _eprint:
702 <https://doi.org/10.3402/tellusa.v2i4.8603>.
- 703 D. Rodrigues, M. C. Alvarez-Castro, G. Messori, P. Yiou, Y. Robin, and D. Faranda. Dynamical
704 Properties of the North Atlantic Atmospheric Circulation in the Past 150 Years in CMIP5 Models
705 and the 20CRv2c Reanalysis. *Journal of Climate*, 31(15):6097–6111, Aug. 2018. ISSN 0894-
706 8755, 1520-0442. doi: 10.1175/JCLI-D-17-0176.1. URL <https://journals.ametsoc>.

- 707 [org/view/journals/clim/31/15/jcli-d-17-0176.1.xml](https://journals.clim/31/15/jcli-d-17-0176.1.xml). Publisher: American Meteorological Society Section: Journal of Climate.
- 708
- 709 E. Rousi, K. Kornhuber, G. Beobide-Arsuaga, F. Luo, and D. Coumou. Accelerated western
710 European heatwave trends linked to more-persistent double jets over Eurasia. *Nature Com-*
711 *munications*, 13(1):3851, July 2022. ISSN 2041-1723. doi: 10.1038/s41467-022-31432-y.
712 URL <https://www.nature.com/articles/s41467-022-31432-y>. Number: 1 Publisher:
713 Nature Publishing Group.
- 714 A. A. Scaife, T. Woollings, J. Knight, G. Martin, and T. Hinton. Atmospheric Blocking and Mean
715 Biases in Climate Models. *Journal of Climate*, 23(23):6143–6152, Dec. 2010. ISSN 0894-
716 8755, 1520-0442. doi: 10.1175/2010JCLI3728.1. URL [https://journals.ametsoc.org/
717 view/journals/clim/23/23/2010jcli3728.1.xml](https://journals.ametsoc.org/view/journals/clim/23/23/2010jcli3728.1.xml). Publisher: American Meteorological
718 Society Section: Journal of Climate.
- 719 S. I. Seneviratne, X. Zhang, M. Adnan, W. Badi, C. Dereczynski, A. Di Luca, S. Ghosh, I. Iskandar,
720 J. Kossin, S. Lewis, F. Otto, I. Pinto, M. Satoh, S. M. Vicente-Serrano, M. Wehner, and B. Zhou.
721 Weather and climate extreme events in a changing climate. In V. Masson-Delmotte, P. Zhai,
722 A. Pirani, S. L. Connors, C. Péan, S. Berger, N. Caud, Y. Chen, L. Goldfarb, M. I. Gomis,
723 M. Huang, K. Leitzell, E. Lonnoy, J. B. R. Matthews, T. K. Maycock, T. Waterfield, Yelekçi,
724 R. Yu, and B. Zhou, editors, *Climate Change 2021: The Physical Science Basis. Contribution
725 of Working Group I to the Sixth Assessment Report of the Intergovernmental Panel on Climate
726 Change*, pages 1513–1766. Cambridge University Press, Cambridge, United Kingdom and New
727 York, NY, USA, 2021. doi: 10.1017/9781009157896.001.
- 728 N. C. Stenseth, G. Ottersen, J. W. Hurrell, A. Mysterud, M. Lima, K. Chan, N. G. Yoccoz,
729 and B. Ådlandsvik. Studying climate effects on ecology through the use of climate indices:
730 the North Atlantic Oscillation, El Niño Southern Oscillation and beyond. *Proceedings of the
731 Royal Society of London. Series B: Biological Sciences*, 270(1529):2087–2096, Oct. 2003.
732 doi: 10.1098/rspb.2003.2415. URL [https://royalsocietypublishing.org/doi/abs/
733 10.1098/rspb.2003.2415](https://royalsocietypublishing.org/doi/abs/10.1098/rspb.2003.2415). Publisher: Royal Society.
- 734 N. C. Swart, J. N. S. Cole, V. V. Kharin, M. Lazare, J. F. Scinocca, N. P. Gillett, J. Anstey,
735 V. Arora, J. R. Christian, S. Hanna, Y. Jiao, W. G. Lee, F. Majaess, O. A. Saenko, C. Seiler,

- 736 C. Seinen, A. Shao, M. Sigmond, L. Solheim, K. von Salzen, D. Yang, and B. Winter. The
737 Canadian Earth System Model version 5 (CanESM5.0.3). *Geoscientific Model Development*, 12
738 (11):4823–4873, Nov. 2019. ISSN 1991-959X. doi: 10.5194/gmd-12-4823-2019. URL <https://gmd.copernicus.org/articles/12/4823/2019/>. Publisher: Copernicus GmbH.
- 740 H. Tatebe, T. Ogura, T. Nitta, Y. Komuro, K. Ogochi, T. Takemura, K. Sudo, M. Sekiguchi, M. Abe,
741 F. Saito, M. Chikira, S. Watanabe, M. Mori, N. Hirota, Y. Kawatani, T. Mochizuki, K. Yoshimura,
742 K. Takata, R. O’ishi, D. Yamazaki, T. Suzuki, M. Kurogi, T. Kataoka, M. Watanabe, and
743 M. Kimoto. Description and basic evaluation of simulated mean state, internal variability, and
744 climate sensitivity in MIROC6. *Geoscientific Model Development*, 12(7):2727–2765, July 2019.
745 ISSN 1991-959X. doi: 10.5194/gmd-12-2727-2019. URL <https://gmd.copernicus.org/articles/12/2727/2019/>. Publisher: Copernicus GmbH.
- 747 D. Valle, P. Albuquerque, Q. Zhao, A. Barberan, and R. J. Fletcher Jr. Extend-
748 ing the Latent Dirichlet Allocation model to presence/absence data: A case study on
749 North American breeding birds and biogeographical shifts expected from climate change.
750 *Global Change Biology*, 24(11):5560–5572, 2018. ISSN 1365-2486. doi: 10.1111/
751 gcb.14412. URL <https://onlinelibrary.wiley.com/doi/abs/10.1111/gcb.14412>.
752 _eprint: <https://onlinelibrary.wiley.com/doi/pdf/10.1111/gcb.14412>.
- 753 G. J. van Oldenborgh, S. Drijfhout, A. van Ulden, R. Haarsma, A. Sterl, C. Severijns, W. Hazeleger,
754 and H. Dijkstra. Western Europe is warming much faster than expected. *Climate of the Past*,
755 5(1):1–12, Jan. 2009. ISSN 1814-9324. doi: 10.5194/cp-5-1-2009. URL <https://cp.copernicus.org/articles/5/1/2009/>. Publisher: Copernicus GmbH.
- 757 R. Vautard. Multiple Weather Regimes over the North Atlantic: Analysis of Pre-
758 cursors and Successors. *Monthly Weather Review*, 118(10):2056–2081, Oct. 1990.
759 ISSN 1520-0493, 0027-0644. doi: 10.1175/1520-0493(1990)118<2056:MWROTN>2.0.CO;
760 2. URL https://journals.ametsoc.org/view/journals/mwre/118/10/1520-0493_1990_118_2056_mwrotn_2_0_co_2.xml. Publisher: American Meteorological Society Sec-
761 tion: Monthly Weather Review.
- 763 R. Vautard, J. Cattiaux, T. Happé, J. Singh, R. Bonnet, C. Cassou, D. Coumou, F. D’Andrea,
764 D. Faranda, E. Fischer, A. Ribes, P. Yiou, and S. Sippel. Heat extremes in Western Europe are

765 increasing faster than simulated due to missed atmospheric circulation trends, Jan. 2023a. URL
766 <https://hal.science/hal-03937057>.

767 R. Vautard, G. J. van Oldenborgh, R. Bonnet, S. Li, Y. Robin, S. Kew, S. Philip, J.-M. Soubeyrou,
768 B. Dubuisson, N. Viovy, M. Reichstein, F. Otto, and I. Garcia de Cortazar-Atauri. Human
769 influence on growing-period frosts like in early April 2021 in central France. *Natural Hazards
770 and Earth System Sciences*, 23(3):1045–1058, Mar. 2023b. ISSN 1561-8633. doi: 10.5194/
771 nhess-23-1045-2023. URL <https://nhess.copernicus.org/articles/23/1045/2023/>.
772 Publisher: Copernicus GmbH.

773 J. M. Wallace and P. V. Hobbs. *Atmospheric science: an introductory survey*, volume 92. Elsevier,
774 2006.

775 V. Weilhhammer, J. Schmid, I. Mittermeier, F. Schreiber, L. Jiang, V. Pastuhovic, C. Herr, and
776 S. Heinze. Extreme weather events in europe and their health consequences – A systematic
777 review. *International Journal of Hygiene and Environmental Health*, 233:113688, Apr. 2021.
778 ISSN 1438-4639. doi: 10.1016/j.ijheh.2021.113688. URL [https://www.sciencedirect.
779 com/science/article/pii/S1438463921000018](https://www.sciencedirect.com/science/article/pii/S1438463921000018).

780 T. Ziehn, M. A. Chamberlain, R. M. Law, A. Lenton, R. W. Bodman, M. Dix, L. Stevens, Y.-P. Wang,
781 J. Srbinovsky, T. Ziehn, M. A. Chamberlain, R. M. Law, A. Lenton, R. W. Bodman, M. Dix,
782 L. Stevens, Y.-P. Wang, and J. Srbinovsky. The Australian Earth System Model: ACCESS-
783 ESM1.5. *Journal of Southern Hemisphere Earth Systems Science*, 70(1):193–214, Aug. 2020.
784 ISSN 2206-5865, 2206-5865. doi: 10.1071/ES19035. URL [https://www.publish.csiro.
785 au/es/ES19035](https://www.publish.csiro.au/es/ES19035). Publisher: CSIRO PUBLISHING.